

Final Technical Report

Contract Number: **FA9101-15-D-0005**

Contract Period 9/01/17-5/30/19

Project Title: **Task No. 17-01**

**Development and Implementation of
an Unsteady Force and Movement
Measurement System into Hypersonic
Wind Tunnel 9**

Principal Investigator: **Sung W. Lee**
Professor
Dept. of Aerospace Engineering
University of Maryland
College Park, MD 20742
Phone: (301) 405-1128
swlee@umd.edu

Contents:

1. Summary
2. Force reconstruction with FDIM with multiple calibration tests

REPORT DOCUMENTATION PAGE

Form Approved
OMB No. 0704-0188

The public reporting burden for this collection of information is estimated to average 1 hour per response, including the time for reviewing instructions, searching existing data sources, gathering and maintaining the data needed, and completing and reviewing the collection of information. Send comments regarding this burden estimate or any other aspect of this collection of information, including suggestions for reducing the burden, to the Department of Defense, Executive Service Directorate (0704-0188). Respondents should be aware that notwithstanding any other provision of law, no person shall be subject to any penalty for failing to comply with a collection of information if it does not display a currently valid OMB control number.

PLEASE DO NOT RETURN YOUR FORM TO THE ABOVE ORGANIZATION.

1. REPORT DATE (DD-MM-YYYY) 17-10-2019		2. REPORT TYPE Final		3. DATES COVERED (From - To) 01-09-2017 to 30-05-2019	
4. TITLE AND SUBTITLE DEVELOPMENT AND IMPLEMENTATION OF AN UNSTEADY FORCE AND MOMENT MEASUREMENT SYSTEM INTO HYPERSONIC WIND TUNNEL 9 AEDC/White Oak Projects Team Assistant Engineer -- Task 17-01				5a. CONTRACT NUMBER FA9101-15-D-0005	
				5b. GRANT NUMBER	
				5c. PROGRAM ELEMENT NUMBER	
6. AUTHOR(S) SUNG W LEE				5d. PROJECT NUMBER	
				5e. TASK NUMBER UMD TASK ORDER 17-01	
				5f. WORK UNIT NUMBER	
7. PERFORMING ORGANIZATION NAME(S) AND ADDRESS(ES) UNIVERSITY OF MARYLAND 3112 LEE BUILDING COLLEGE PARK, MD 20742				8. PERFORMING ORGANIZATION REPORT NUMBER	
9. SPONSORING/MONITORING AGENCY NAME(S) AND ADDRESS(ES) AFTC/PZI (ARNOLD) 100 KINDEL DRIVE, SUITE A-332 ARNOLD AFB, TN 37389-1332 PATRICIA L HENDERSON patricia.henderson.2@us.af.mil				10. SPONSOR/MONITOR'S ACRONYM(S)	
				11. SPONSOR/MONITOR'S REPORT NUMBER(S)	
12. DISTRIBUTION/AVAILABILITY STATEMENT					
13. SUPPLEMENTARY NOTES					
14. ABSTRACT Dynamic force measurement methodologies were developed for potential use in AEDC's Hypervelocity Tunnel No. 9. They are the Time Domain Deconvolution Method (TDDM), Frequency Domain Inverse Method (FDIM) and Sum of Weighted Acceleration Technique (SWAT). The effectiveness of each method was validated both on numerical spring-mass-damper systems as well as on a test article in the Balance Calibration Laboratory at Tunnel 9. The new TDDM developed allows for stable solution without the need for conventional regularization of the inverse problem. FDIM with multiple calibration tests significantly reduces the effect of experimental noise as the number of calibration increases, expanding the applicability of this method. Also, SWAT with modal separation offers improvement over the conventional SWAT.					
15. SUBJECT TERMS					
16. SECURITY CLASSIFICATION OF:			17. LIMITATION OF ABSTRACT UU	18. NUMBER OF PAGES 238	19a. NAME OF RESPONSIBLE PERSON SUNG W LEE
a. REPORT U	b. ABSTRACT U	c. THIS PAGE U			19b. TELEPHONE NUMBER (Include area code) 301-405-1128

Reset

1. Summary

Dynamic force measurement methodologies were developed for potential use in AEDC's Hypervelocity Tunnel No. 9. They are the Time Domain Deconvolution Method (TDDM), Frequency Domain Inverse Method (FDIM) and Sum of Weighted Acceleration Technique (SWAT). The effectiveness of each method was validated both on numerical spring-mass-damper systems as well as on a test article in the Balance Calibration Laboratory at Tunnel 9.

To improve the performance of SWAT, modal separation and a damping matrix was added to the formulation to allow for high frequency modal amplitude reduction where the conventional method showed significant, undesirable modal amplification.

A novel TDDM was developed based on the convolution relationship between input and output. In this new approach, an impulse response function is assumed to be linear or cubic over each time segment as in the finite element formulation. The time segment for the impulse response function can be selected as an integer multiple of the time segment for input/ output sampling. This allows for stable solution of the deconvolution problem without the need for conventional regularization of the inverse problem. Additionally, considering only a small segment of the output at a time, large segment can be reconstructed in a more reasonable amount of time.

The FDIM was also reformulated for direct solution of the frequency response function (FRF) through the use of multiple calibration tests. It is shown that the new approach helps reduce significantly the effect of experimental error and noise as the number of calibration tests increases, expanding the applicability of this method. The result of this investigation is included in this report.

The work conducted through this project has resulted in a Ph.D. dissertation (by John Draper III) and two journal papers as follows:

Journal papers published:

Draper, J.W., Lee, S.W. and Marineau, E.C., 'Numerical Construction of Impulse Response Functions and Input Signal Reconstruction,' *J. Sound and Vibration*, vol 432, 259–271, 2018.

Draper, J.W. and Lee, S.W., 'Smooth Construction of Impulse Response Functions and Applied Loads using a Time Domain Deconvolution Method,' *J. Sound and Vibration*, vol. 443, pp. 430–443, 2019.

Force Reconstruction via FDIM with Multiple Calibration Tests

Jack Draper

October 6, 2019

1 Introduction

Inverse signal reconstruction is an interest in many fields such as force, heat flux[18], and acoustic[?] measurement. One often wishes to observe a quantity that is not directly measurable or proportional to a measurable quantity. In this paper, we refer to these measurements as "dynamic" and the reconstruction of such quantities requires more elegant techniques.

The chief focus for this work is dynamic force measurement. The authors seek an effective method for measuring transient, high frequency, or unsteady forcing in hypersonic wind tunnels. This work is intended to support future implementation of dynamic force measurement at the Arnold Engineering Development Complex's (AEDC) Hypervelocity Wind Tunnel No. 9[9]. There are many relevant applications of dynamic force measurement in hypersonic wind tunnel testing. Examples include jet-flow interaction[6, 8], scramjet engine unstart[10, 11], and control surface deployment[12, 5]. As the development of flightworthy hypersonic vehicles continues to mature, so too will the need for measurement of these transient phenomenon.

Many techniques are relevant to this applications. For example, Draper et al. applied an extension to the typically used static calibration methodology[7] known as the sum of weighted accelerations technique (SWAT)[2]. In this method, modally separated acceleration measurements are used to remove the inertial response from the statically calibrated response. However, sensor response delay band limited the effectiveness of the SWAT to approximately 200 Hz. Researchers

at the CALSPAN-University of Buffalo Research Center (CUBRC) for example, also used an acceleration compensated strain measurement to remove the inertial response[14, 13]. Deconvolution methods are also very applicable for point force applications. Draper et al.[3] developed a linearized time domain solution of the convolution problem and then generalized this formulation to any order[4]. Many other time domain deconvolution methods (TDDMs) exist and are arguably the most popular approach to force reconstruction. For example a TDDM was utilized by researchers at the University of Queensland to measure startup drag on a slender test article in a shock tunnel[16, 15].

One major drawback of TDDMs is the computational expense of the formulation. The size of the matrix to be inverted grows as the length of the time history squared. Therefore, the computational effort can be excessive for long time histories (e.g. many seconds) sampled in the kilohertz range. To circumvent this limitation, the frequency domain couple to TDDM is often employed. This is referred to as the frequency domain inverse method (FDIM). For example researchers at NASA Ames Research Center attempted to reconstruct unsteady aerodynamic forcing on a launch vehicle[17]. However, they noted a difficulty in accurately reconstructing the frequency response functions which caused an inability to accurately isolate unsteady aerodynamic loads.

Expanding the capability of the FDIM is the primary focus of this work. In particular, we choose to directly solve for the frequency response function (FRF). Although this alone can cause noise amplification, this formulation allows for the use of multiple calibration inputs which ultimately can reduce the influence of user error and noise. Additionally, the application of this method on acceleration responses is shown. In the first section, the conventional FDIM and the alterations in this paper are presented. Following this, a numerical validation is performed on single and multiple degree of freedom systems to highlight some of the advantages of the alterations. Finally, the methods are validated on an experimental system in AEDC's Balance Calibration Laboratory.

2 Formulation

In this section, we present the typical FDIM for solution of dynamic forces. Following this, we present a new approach to dynamic calibration that allows for less reliance on a single test.

2.1 Conventional FDIM

We begin with the convolution integral that relates the input, $u(t)$, and output, $y(t)$, via a convolution with the impulse response function (IRF), $h(t)$. The continuous form of this expression for a system initially at rest is given as

$$y(t) = \int_0^t h(t - \tau)u(\tau)d\tau. \quad (1)$$

To solve this using the FDIM, a Fourier Transform is performed on Eq. (1). If this is done, the result is given by

$$Y(\omega) = H(\omega) \cdot U(\omega) \quad (2)$$

where capital variables signify frequency domain functions. Note that the complex convolution of two time domain functions has become a more simple multiplication of two frequency domain functions.

Typical solution for the IRF invokes the assumption that system response to a finite pulse is approximately the impulse response[15]. If the response is scaled by the area and time shifted by half the width of the pulse, this is a decent assumption. Any output response can be deconvolved with this impulse response to reconstruct the input. To appreciate this, observe Figure 1. The

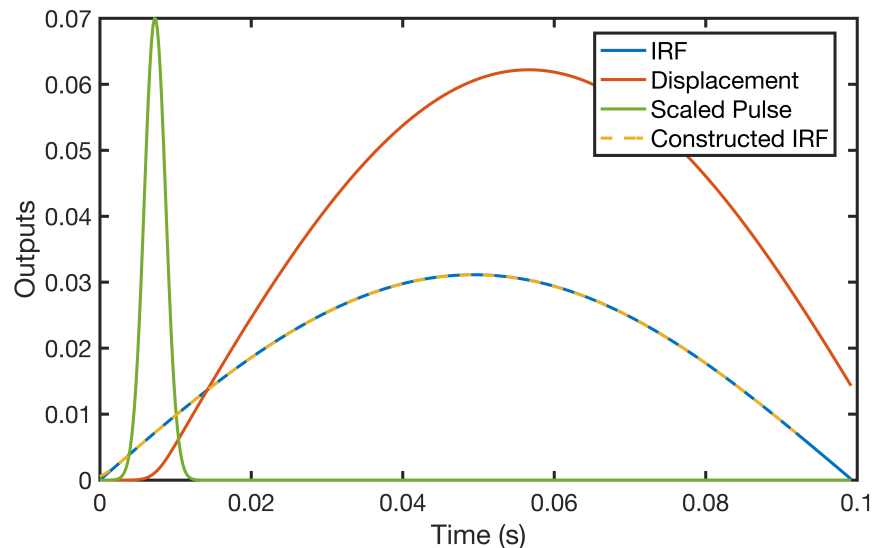


Figure 1: Typical IRF solution using scaling and time shifting of the displacement.

unaltered output (red) from the applied finite pulse does not appear to match the analytical IRF.

However, when the displacement is scaled by the area under the pulse and shifted by half of the width of the pulse, it nearly perfectly matches the analytical IRF. Note that the magnitude of the pulse has been reduced considerably for visualization purposes.

With the IRF known, one may utilize the discrete Fourier Transform (DFT) to convert the IRF into the frequency domain. This is commonly referred to as the FRF. Next, one may measure a response caused by an applied dynamic load. Again using the DFT, one may obtain the frequency domain couple to the output (i.e. $Y(\omega)$).

Finally, to obtain the unknown applied force, one may perform a piecewise division of the output by the FRF at every frequency, i.e.

$$U(\omega) = \frac{Y(\omega)}{H(\omega)}. \quad (3)$$

The time domain couple to this input force is obtained using the inverse discrete Fourier Transform (IDFT).

One may note that since a division is required rather than a matrix inversion, this operation requires $\mathcal{O}(N)$ operations rather than $\mathcal{O}(N^2)$ where N is the length of a measured channel. As expected, the computational efficiency has increased significantly and much longer time segments can be deconvolved.

Alternatively, Eq. (2) could be solved for $H(\omega)$ given a measured input and output. However, the former approach is usually taken for simplicity. Additionally, instrumented impulse hammers are commercially available and therefore the determination of area and pulse width is simple.

In the SIMO case, the solution is obtained in a very similar fashion to the conventional FDIM. Begin by obtaining all FRFs between the input location and all output channels. For the conventional FDIM, this is obtained by performing a Fourier transform on the scaled and time shifted output to an applied hammer pulse. Each FRF at a frequency is denoted as $(H_j)_\omega$ and the Fourier Transform of each measured output at a particular frequency $(Y_j)_\omega$, where the output location is denoted by the subscript j and the frequency of interest is denoted by the subscript ω . Note, reconstruction of the input force requires information from all outputs. Therefore, Eq. (2) is stacked

for all output locations to obtain

$$\begin{pmatrix} Y_1 \\ Y_2 \\ \vdots \\ Y_M \end{pmatrix}_\omega = \begin{pmatrix} H_1 \\ H_2 \\ \vdots \\ H_M \end{pmatrix}_\omega U(\omega) \quad (4)$$

or in compact form as

$$\mathbf{Y}(\omega) = \mathbf{H}(\omega)U(\omega) \quad (5)$$

which holds for every frequency, ω . Note that M represents the arbitrary number of output channels used for the reconstruction.

Since this is a matrix equation, point wise division is no longer applicable. However, a simple least squares inversion can once again be used to solve for the input force as

$$U(\omega) = \mathbf{H}^+(\omega)\mathbf{Y}(\omega). \quad (6)$$

This is evaluated at each frequency which requires much less computation time compared to a typical TDDM.

Finally, a scenario where the force reconstruction at multiple input locations is of interest is considered. Such scenarios may be referred to as MIMO. As in the TDDMs, the MIMO formulation is simply a superposition of SIMO formulations. This is represented as

$$\begin{pmatrix} Y_1 \\ Y_2 \\ \vdots \\ Y_M \end{pmatrix}_\omega = \begin{bmatrix} H_{11} & H_{12} & \dots & H_{1P} \\ H_{21} & H_{22} & \dots & H_{2P} \\ \vdots & \vdots & \ddots & \vdots \\ H_{M1} & H_{M2} & \dots & H_{MP} \end{bmatrix}_\omega \begin{pmatrix} U_1 \\ U_2 \\ \vdots \\ U_P \end{pmatrix}_\omega \quad (7)$$

where P input locations are of interest. Again this is represented in compact form as

$$\mathbf{Y}(\omega) = \mathcal{H}(\omega)\mathbf{U}(\omega) \quad (8)$$

and solved using a least squares pseudo inverse as

$$\mathbf{U}(\omega) = \mathcal{H}^+(\omega)\mathbf{Y}(\omega) \quad (9)$$

provided $M > P$.

If N frequencies are of interest, this requires the pseudo inversion of N $M \times P$ matrices. Since inversion is $\mathcal{O}(P^3)$ for this inversion, the MIMO computation is $\mathcal{O}(N \cdot P^3)$. The inversion for the typical MIMO TDDM is $\mathcal{O}(N^3 \cdot P^3)$, a factor of N^2 larger. The computational efficiency of the FDIM is obvious as N becomes large.

2.2 FRF Solution

In this section, the assumption of the IRF being equivalent to a multiple of the response to a hammer pulse is no longer made. Rather, the convolution relationship is solved in the frequency domain with a known applied load and measured response.

Return to Eq. (2) with $U(\omega)$ known (measured) and the FRF unknown. As in the solution of an unknown applied force, the solution of the FRF is simply a division of the output by the input at each frequency, i.e.

$$H(\omega) = \frac{Y(\omega)}{U(\omega)}. \quad (10)$$

Although this formulation requires more computation than the conventional one (i.e. assuming the measured response to a pulse loading is proportional to the FRF), this formulation is required for the alternative approach to be presented in the next section. Additionally, this allows for a variety of calibration load types as opposed to just pulses.

2.3 Use of Multiple Calibration Sets

In this section, we again assume the FRF of the system is not dependent on the applied load. That means that any applied load at a particular location should exhibit an identical FRF as any other load applied at the same location. This is capitalized upon to reduce the ill effects of noise amplification by performing multiple calibration tests. This approach is similar in spirit to that performed by Draper et al. on their TDDM[?] but this time applied to a FDIM.

Applying p input calibration tests at the same location results in

$$\begin{pmatrix} Y_1 \\ Y_2 \\ \vdots \\ Y_p \end{pmatrix}_\omega = \begin{pmatrix} U_1 \\ U_2 \\ \vdots \\ U_p \end{pmatrix}_\omega H(\omega) \quad (11)$$

at each frequency and written compactly as

$$\mathbf{Y}(\omega) = \mathbf{U}(\omega)H(\omega). \quad (12)$$

Since the noise is random from test to test, utilizing repeat tests will hopefully result in a more accurate FRF construction. As in Eq. (6), the FRF is solved using a least squares pseudo inverse as

$$H(\omega) = \mathbf{U}^+(\omega)\mathbf{Y}(\omega). \quad (13)$$

Since each FRF is unique, this technique can be repeated for solving for the FRF at each input-output pair when considering the SIMO or MIMO case.

2.4 Acceleration Deconvolution

In this section, we show the differentiability of the convolution integral, i.e.

$$\frac{d}{dt}y(t) = \frac{d}{dt}h * u(t) \quad (14)$$

or in compact notation as

$$\dot{y}(t) = \dot{h} * u(t) \quad (15)$$

where the dot signifies a time derivative and $*$ represents the convolution operation. Obviously, using the commutative property of the convolution, we could apply the time derivative to the function $u(t)$ instead. However, applying the derivative to $h(t)$ is more useful for the applications discussed in this paper.

This property is most easily derived using the inverse Fourier Transform, i.e.

$$f(t) = \int_{-\infty}^{\infty} \exp^{2\pi i\omega t} F(\omega) d\omega \quad (16)$$

which transforms frequency domain signals back to the time domain. Evaluating the time derivative of Eq. (16) we obtain

$$\dot{f} = \frac{d}{dt} \int_{-\infty}^{\infty} \exp^{2\pi i\omega t} F(\omega) d\omega = 2\pi i\omega \int_{-\infty}^{\infty} \exp^{2\pi i\omega t} F(\omega) d\omega. \quad (17)$$

Hence the Fourier Transform of the time derivative of an arbitrary function is

$$\mathcal{F} \left\{ \dot{f}(t) \right\} = 2\pi i\omega F(\omega). \quad (18)$$

Returning to Eq. (15), we may apply the Fourier Transform to gain additional insight, i.e.

$$\mathcal{F}\{y(t)\} = 2\pi i\omega \mathcal{F}\{y(t)\} = 2\pi i\omega \mathcal{F}\{h * u(t)\} = 2\pi i\omega H(\omega) \cdot U(\omega). \quad (19)$$

Performing an inverse Fourier Transform results in Eq. (15).

One may also note that this operation is repeatable so long as a differential exists. Therefore, we may repeat this operation to prove

$$\ddot{y}(t) = \ddot{h} * u(t) \quad (20)$$

and all subsequent time derivatives.

Acceleration measurements are significantly easier to obtain than strain/displacement. For strain, one typically needs to ensure all load can travel through the strain gages which often requires designing around sensors. Alternatively, accelerometers need be simply placed on a surface of the body. Therefore acceleration measurement can offer more design flexibility. Additionally, force measurement can theoretically be made without the need for complex strain balances. This may be advantageous in smaller tunnels or small budget experiments.

Returning to our continuous convolution of displacement and applied force, both sides are differentiated twice to obtain Eq. (20).

The unknown is now the acceleration FRF ($\ddot{H}(\omega)$) rather than the typical displacement/strain FRF ($H(t)$). Using the FDIM, one may construct the acceleration FRF and then use it to reconstruct an arbitrary applied dynamic force $u(t)$.

It also should be noted that all of the previously mentioned extensions to the developed FDIM variant are completely applicable to acceleration deconvolution as well. Therefore multiple input tests are used at the same location to solve for the acceleration FRFs. Therefore Eq. (11) becomes

$$\begin{pmatrix} \ddot{Y}_1 \\ \ddot{Y}_2 \\ \vdots \\ \ddot{Y}_p \end{pmatrix}_\omega = \begin{pmatrix} U_1 \\ U_2 \\ \vdots \\ U_p \end{pmatrix}_\omega \ddot{H}(\omega). \quad (21)$$

To solve for the unknown applied load using acceleration-only deconvolution, all of the accel-

eration FRFs are used in the solution. Therefore, the SIMO form becomes

$$\begin{pmatrix} \ddot{Y}_1 \\ \ddot{Y}_2 \\ \vdots \\ \ddot{Y}_{na} \end{pmatrix}_\omega = \begin{pmatrix} \ddot{H}_1 \\ \ddot{H}_2 \\ \vdots \\ \ddot{H}_{na} \end{pmatrix}_\omega U(\omega) \quad (22)$$

where na denotes the number of accelerometers. Additionally, the MIMO formulation becomes

$$\begin{pmatrix} \ddot{Y}_1 \\ \ddot{Y}_2 \\ \vdots \\ \ddot{Y}_{na} \end{pmatrix}_\omega = \begin{bmatrix} \ddot{H}_{11} & \ddot{H}_{12} & \dots & \ddot{H}_{1P} \\ \ddot{H}_{21} & \ddot{H}_{22} & \dots & \ddot{H}_{2P} \\ \vdots & \vdots & \ddots & \vdots \\ \ddot{H}_{na,1} & \ddot{H}_{na,2} & \dots & \ddot{H}_{na,P} \end{bmatrix}_\omega \begin{pmatrix} U_1 \\ U_2 \\ \vdots \\ U_P \end{pmatrix}_\omega. \quad (23)$$

Note the similarity with Eq. (7). Although acceleration measurements are used, the solution methodology is functionally equivalent.

2.5 Combined Acceleration-Strain Deconvolution

Finally, one may note that Eqs.(7) and (23) both solve for the same input forces. Therefore, all of the FRFs are used in the solution. The SIMO form then becomes

$$\begin{pmatrix} Y_1 \\ Y_2 \\ \vdots \\ Y_{ns} \\ \ddot{Y}_1 \\ \ddot{Y}_2 \\ \vdots \\ \ddot{Y}_{na} \end{pmatrix}_\omega = \begin{pmatrix} H_1 \\ H_2 \\ \vdots \\ H_{ns} \\ \ddot{H}_1 \\ \ddot{H}_2 \\ \vdots \\ \ddot{H}_{na} \end{pmatrix}_\omega U(\omega) \quad (24)$$

where ns denotes the number of strain sensors and na denotes the number of accelerometers. Additionally, the MIMO formulation becomes

$$\begin{pmatrix} Y_1 \\ Y_2 \\ \vdots \\ Y_{ns} \\ \ddot{Y}_1 \\ \ddot{Y}_2 \\ \vdots \\ \ddot{Y}_{na} \end{pmatrix}_\omega = \begin{bmatrix} H_{11} & H_{12} & \dots & H_{1P} \\ H_{21} & H_{22} & \dots & H_{2P} \\ \vdots & \vdots & \ddots & \vdots \\ H_{ns,1} & H_{ns,2} & \dots & H_{ns,P} \\ \ddot{H}_{11} & \ddot{H}_{12} & \dots & \ddot{H}_{1P} \\ \ddot{H}_{21} & \ddot{H}_{22} & \dots & \ddot{H}_{2P} \\ \vdots & \vdots & \ddots & \vdots \\ \ddot{H}_{na,1} & \ddot{H}_{na,2} & \dots & \ddot{H}_{na,P} \end{bmatrix}_\omega \begin{pmatrix} U_1 \\ U_2 \\ \vdots \\ U_P \end{pmatrix}_\omega. \quad (25)$$

Note that adding the acceleration measurements increases the row dimension of the inverted matrix. This in theory should improve performance for a least squares solution.

3 Numerical Validation

In this section a few numerical examples of the FDIM solution approach are presented. Due to the more complex nature of these methods, we begin with the more simple SISO numerical systems. This allows for concrete conclusions about each methodology without the complexity of multiple mode interaction. An example single degree of freedom (SDOF) SISO system is given in Figure 2.

To be consistent with the formulation, the output displacement and input force have been assigned the variables $y(t)$ and $u(t)$, respectively. Assuming constant mass, stiffness, and damping values (i.e. m , k , and c) this system is subject to the differential equation

$$m\ddot{y} + c\dot{y} + ky = u(t) \quad (26)$$

where $m = 1$ kg, $k = 1000$ N/m, and $c = 0.6325$ Ns/m. Additionally, the analytical IRF can be solved as

$$h(t) = \frac{1}{m\omega_d} \exp^{-\sigma t} \sin \omega_d t \quad (27)$$

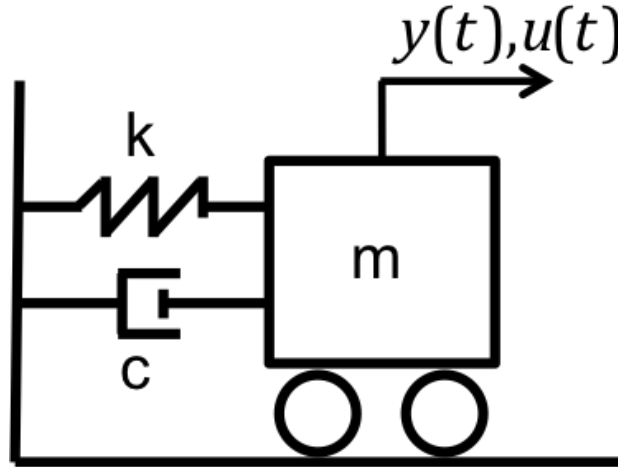


Figure 2: SDOF spring mass damper system.

where

$$\omega_d = \omega_n \sqrt{1 - \zeta^2} \quad (28a)$$

$$\sigma = \zeta \omega_n \quad (28b)$$

and $\omega_n = \sqrt{k/m}$, the natural frequency and $\zeta = c/(2m\omega_n)$, the non-dimensional damping ratio.

The selection of the input calibration force (i.e. the force measured when constructing the IRF) is arbitrary. However, the standard FDIM requires a hammer pulse calibration force. Furthermore, this load is easy to measure using an instrumented impulse hammer. Therefore, in these numerical studies, the chosen calibration force is

$$F(t) = u(t) = \frac{b}{a\sqrt{\pi}} \exp^{-\left(\frac{t-0.5\varepsilon}{a}\right)^2}, \quad (29)$$

where $a = 1 \cdot 10^{-3}$ controls the pulse width, $b = \frac{1}{30}$ is a scaling constant used to select a desired area (and consequently peak magnitude), and ε is the pulse width used to shift the pulse from the $t = 0$ axis. This simulates a steep hammer impulse force with an approximate width of 2 ms and height of 20 N.

Finally, to further simulate experimental studies, Gaussian numerical noise is added to the output data. This additive noise is defined as

$$\varepsilon = \frac{\sigma(\mathbf{y}_e)}{\text{SNR}} \mathbf{randn} \quad (30)$$

where $\sigma(\cdot)$ is the standard deviation operator of the vector of interest, \mathbf{y}_e is the calculated exact output, $\boldsymbol{\varepsilon}$ is a vector of noise values to be added to \mathbf{y}_e , \mathbf{randn} is a vector of points selected from a Gaussian distribution with a standard deviation equal to one, and SNR is the Signal to Noise Ratio defined as

$$\text{SNR} = \frac{\sigma(\mathbf{y}_e)}{\sigma(\mathbf{randn})_{\text{desired}}}. \quad (31)$$

Defining noise in this manner allows the user to supply unbiased noise to the "measured" signal as $\mathbf{y} = \mathbf{y}_e + \boldsymbol{\varepsilon}$ at a desired SNR.

3.1 SISO Example of the Conventional FDIM

The most basic reconstruction problem is first considered. Consider the single input single output (SISO) spring-mass-damper system depicted in Figure 2. Since there is only one output, the SISO case is much less desirable than the single input multiple output (SIMO) case which measures much more information. Only information from one location is available and one cannot over constrain the solution.

Applying the conventional FDIM (i.e. scaling and time shifting output to obtain IRF), the IRF and reconstructed pulse force shown in Figure 3 are obtained. Note that no noise was injected into this problem (aside from unavoidable numerical noise).

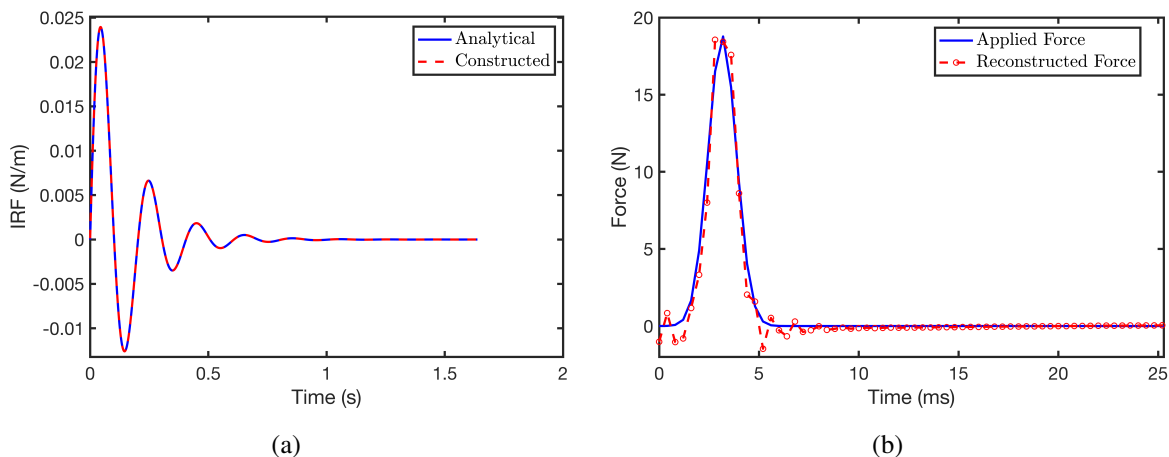


Figure 3: Conventional FDIM noiseless force reconstruction. IRF (a) and reconstructed force (b) are both shown.

As expected, the IRF matches very well with the analytical solution. Furthermore, when this

IRF is used to reconstruct a new load, the reconstruction matches well with the applied load. Note some small errors which can be attributed to numerical error accumulation and inability to perfectly shift the response by half of the impulse width.

Next it is important to observe the detrimental effects of noise to the reconstruction. Repeating the above analysis with $\text{SNR}=150$, the results in Figure 4 are obtained. Although minimal

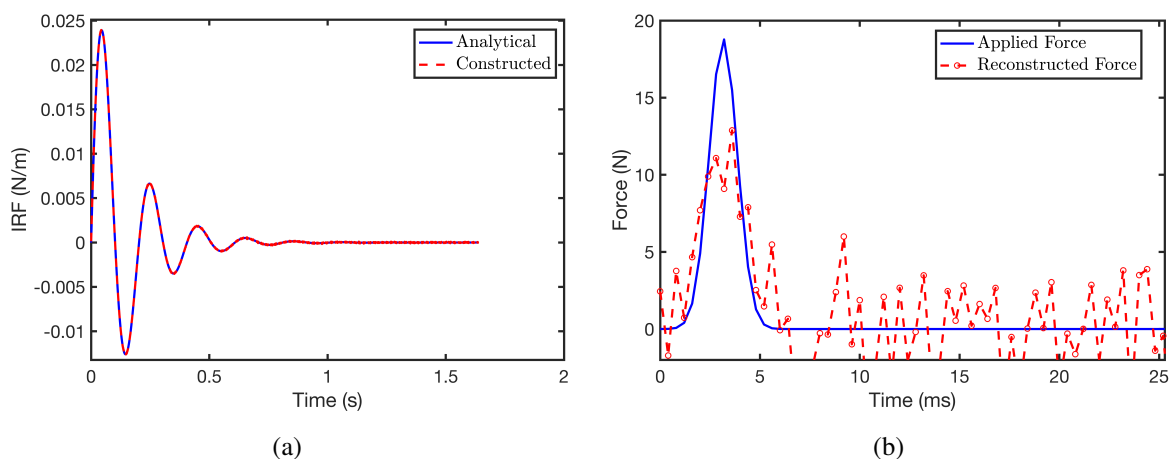


Figure 4: Conventional FDIM noisy force reconstruction. IRF (a) and reconstructed force (b) are both shown.

influence is observed on the FRF solution, large error is present in the pulse force reconstruction. Unfortunately, with this conventional approach, there are no more knobs to turn and one is forced to accept this level of accuracy.

3.2 SISO Example of FDIM with Solved FRF

Next consider the solution of the FRF alteration suggested Section 2.2. Applying this approach, the IRF construction and pulse force reconstruction shown in Figure 5 are obtained.

Again, as expected, the FRF and pulse force are reconstructed with high accuracy. Interestingly, the results actually appear more accurate than the simple scaling of output approach (i.e. Figure 3b). It would seem that solving for the FRF is more accurate than the conventional scaling and time shifting of the response.

Next it is important to observe the detrimental effects of noise to the reconstruction. Repeating the above analysis with $\text{SNR}=150$, the results in Figure 6 are obtained.

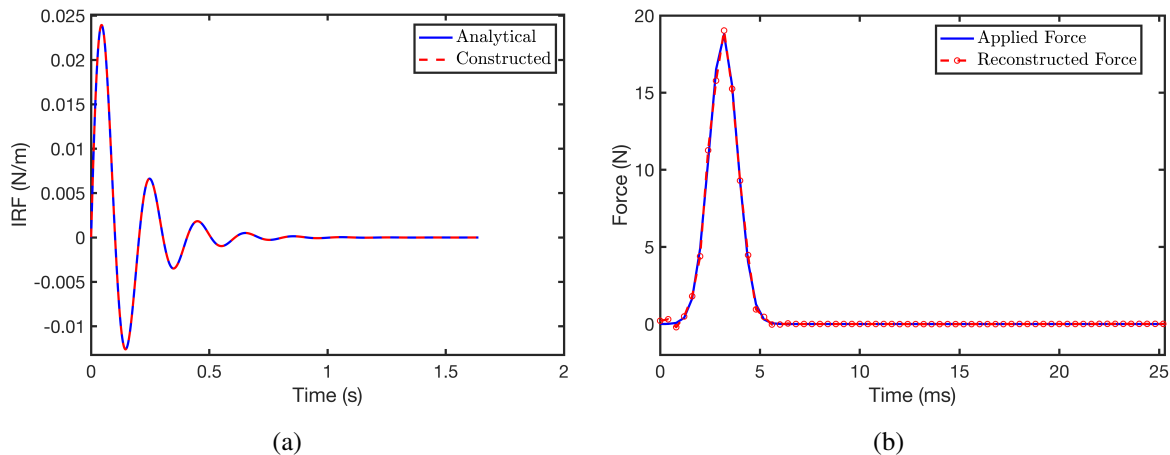


Figure 5: FRF solved FDIM noiseless force reconstruction. IRF (a) and reconstructed force (b) are both shown.

Comparing Figure 6a with Figure 4, it is evident that the FRF solution is worse in the noisy case. Furthermore, if this noisy FRF is used to reconstruct a pulse force, the accuracy is once again unacceptable. The level of error in the reconstructions is comparable with that of the conventional FDIM. Again, no additional alterations are possible for this stage of the method.

3.3 Multiple Calibration Sets

One possible way of increasing accuracy for the FRF construction is by utilizing multiple calibration sets in the FDIM formation. Since each input-output location pair has a unique FRF, one may perform multiple tests and use all of the information to construct the FRF. To compactly observe the influence of repeat tests on FRF construction accuracy, consider Eq. (32)

$$\epsilon = \frac{1}{N} |h_{\text{exact}} - h_{\text{rec}}|^2 \quad (32)$$

and compute this accuracy versus number of calibration tests. A plot of this is shown in Figure 7. Since the FRF often displays high frequency error (e.g. Figure 9b) computing an error metric based on the FRF is often less informative.

Since the FDIM is so computationally efficient, one may perform many numerical studies with very little computational effort. Upon review of Figure 7, a very clear linear trend in log space is evident for the multiple calibration approach. One can achieve about an order of magnitude

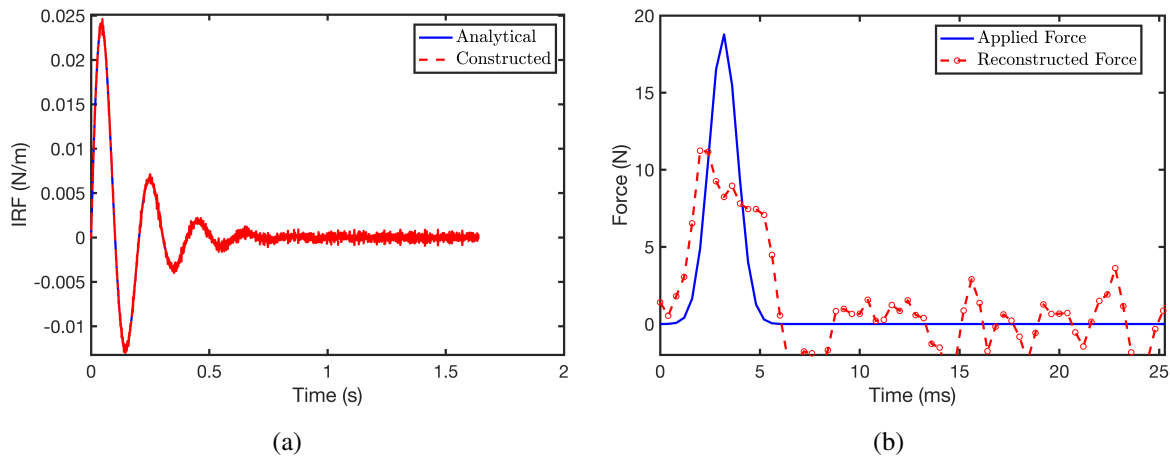


Figure 6: FRF solved FDIM noisy force reconstruction. IRF (a) and reconstructed force (b) are both shown.

decrease in error by increasing the number of calibration tests by about an order of magnitude. Although performing 100+ tests at the same hole location in real life may be unreasonable, it is useful to show that performing multiple tests can improve the accuracy.

Although higher accuracy than the conventional approach is achievable, this method still underperforms for any practical number of tests on this SISO case study. Regardless, this at least gives the tester an option to change where previously they could not.

3.4 SIMO Example

In this section SIMO force reconstruction is presented for a ten DOF lumped mass oscillator. This is ten of the SDOF systems linked together with springs and dampers. The stiffness and damping values were selected randomly from 0-1000 and 0-100, respectively.

The FDIM presented in Section 2.2 is validated here. Using this more simplified method, one may observe the advantages of adding multiple calibration sets later in the section. Using this method, the pulse shown in Figure 8 is obtained.

As expected, excellent accuracy is achieved for the noiseless case. When reviewing the various IRFs, a curious phenomenon is observed. This is shown in Figure 9a. Ringing is present in the beginning and end of the reconstruction. This is primarily due to the large high frequency error in the FRF which is shown in Figure 9b. However, this error does not materialize into large errors in

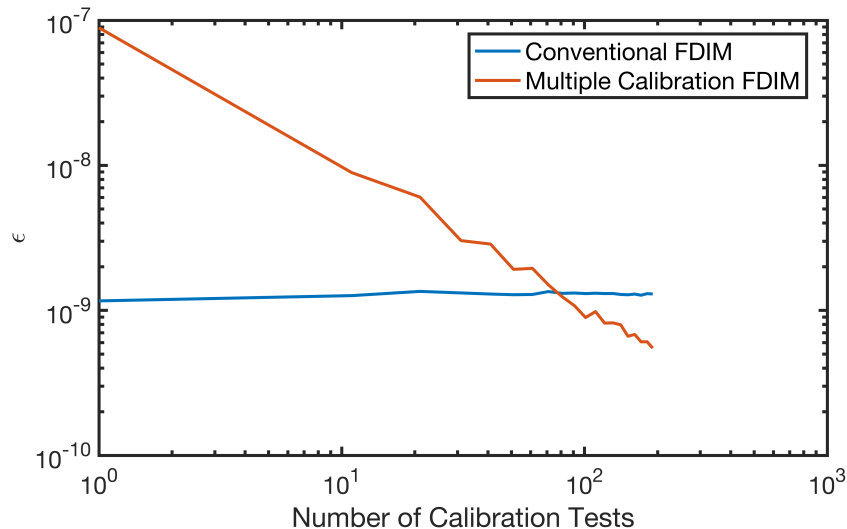


Figure 7: FDIM SISO IRF construction accuracy versus number of calibration tests

the force reconstruction.

This high frequency error in the FRF is due to the finite pulse used for calibration. The Fourier Transform of an infinitesimal width pulse is constant at a value of 1. When a finite pulse is used, this constant value drops off steeply at high frequencies. When the frequency response is divided by the Fourier Transform of the pulse, this manifests as large FRF contributions at high frequencies. This is an unavoidable consequence of using a finite pulse. One may attempt to remedy this by filtering the signal at a value of

$$f_c = \frac{1}{\epsilon} \quad (33)$$

the inverse of the pulse width. For this example, that value is 159 Hz, approximately the value where this steep increase in the FRF begins. For accurate view of the FRF, this filtering is required, however, why this is not required for pulse reconstruction is shown below.

The reconstructed force was a new pulse with different magnitude, pulse width, area, and noise properties than the pulse used for calibration. Therefore, any claim of over fitting is invalid. Clearly the use of the erroneous FRF still yields excellent results for the noiseless case.

Next it is of interest to investigate the negative effects of noise and how it may degrade the results. This is shown in Figure 10. Once again substantial high frequency error is observed in the FRF due to the finite pulse. However, with the presence of noise, the pulse reconstruction is no longer unaffected. Substantial under prediction of the pulse is observed. This trend is consis-

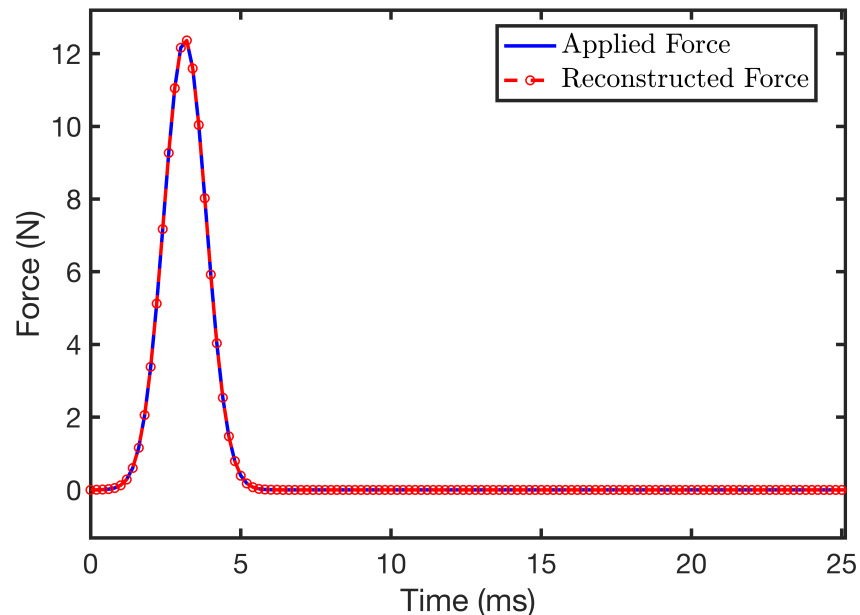


Figure 8: FDIM SIMO noiseless force reconstruction at input DOF 3

tent across many tests with varying sampling frequencies, pulse widths, DOFs, and noise levels. Therefore, one may conclude that noise causes unavoidable error in the FRF solved FDIM. Note that there are slight differences in the analytical FRF from Figure 9b and 10a. This is due to the random selection of system parameters during a particular numerical experiment. However, these trends are very repeatable.

Next multiple calibration tests are incorporated to investigate the repeat formulation. The hypothesis is that with more calibration inputs, a better approximation of the FRF will be obtained resulting in more accurate reconstructions. The results of the same FDIM experiment with ten calibration tests at the same location is shown in Figure 11.

No discernible accuracy increase is evident in Figure 11a, however, the pulse reconstruction is clearly more accurate. To more concretely observe this effect, the force reconstruction for a varying number of input calibration tests is performed and the peak and area difference of each reconstruction is computed. These error metrics are

$$AD = \left| 1 - \frac{\int_0^\varepsilon f_{\text{rec}}(t) dt}{\int_0^\varepsilon f_{\text{app}}(t) dt} \right| \cdot 100\% \quad (34)$$

$$PD = \left| 1 - \frac{\max |f_{\text{rec}}(t)|}{\max |f_{\text{app}}(t)|} \right| \cdot 100\% \quad (35)$$

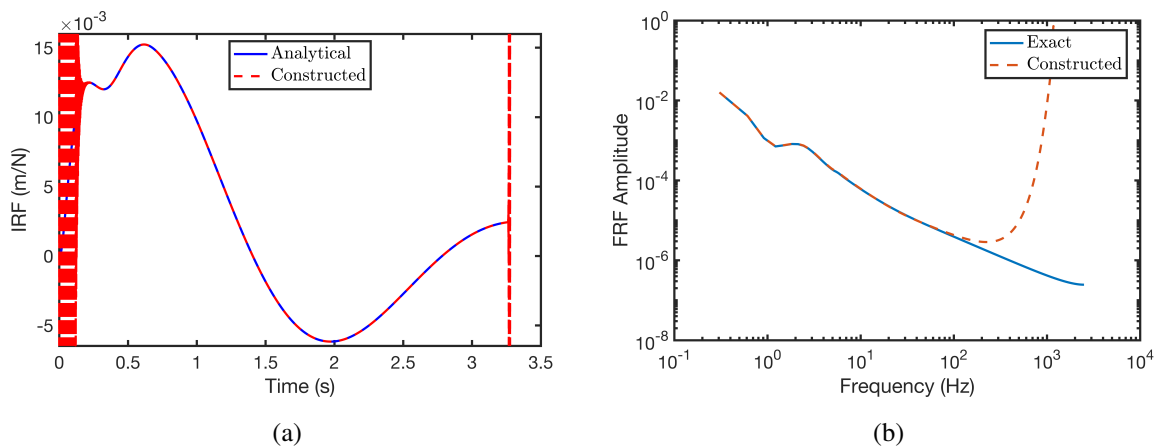


Figure 9: IRF (a) and FRF (b) construction at DOF 5 using FDIM with FRF solution.

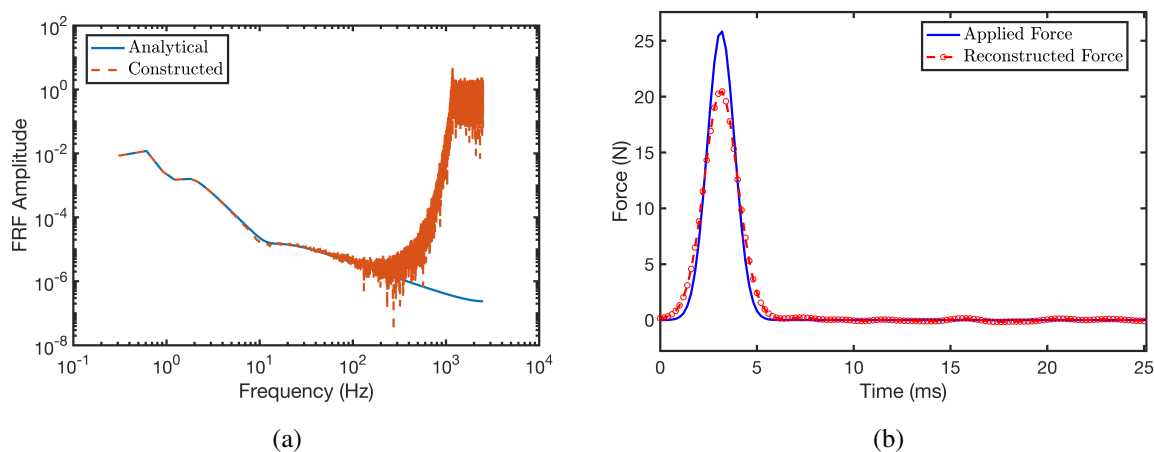


Figure 10: FRF solved SIMO FDIM noisy force reconstruction. FRF at DOF 5 (a) and reconstructed force (b) are both shown. SNR= 150 used for this example.

where AD and PD stand for Area Difference and Peak Difference, respectively. The symbols $f_{\text{app}}(t)$ and $f_{\text{rec}}(t)$ represent the discrete applied and reconstructed force, respectively. Finally, ε is the time width of the specific impulse under investigation; selected to be the location where the magnitude of the pulse drops below an arbitrarily chosen low value of 0.001 N. We use trapezoidal integration to solve for the area as only the points at each sampling interval are known. These error metrics versus the number of calibration inputs are displayed in Figure 12 with varying levels of SNR.

As expected, the peak error reduced considerably when increasing the number of calibration tests. The most substantial accuracy increase occurs after the first few repeat tests. The influence

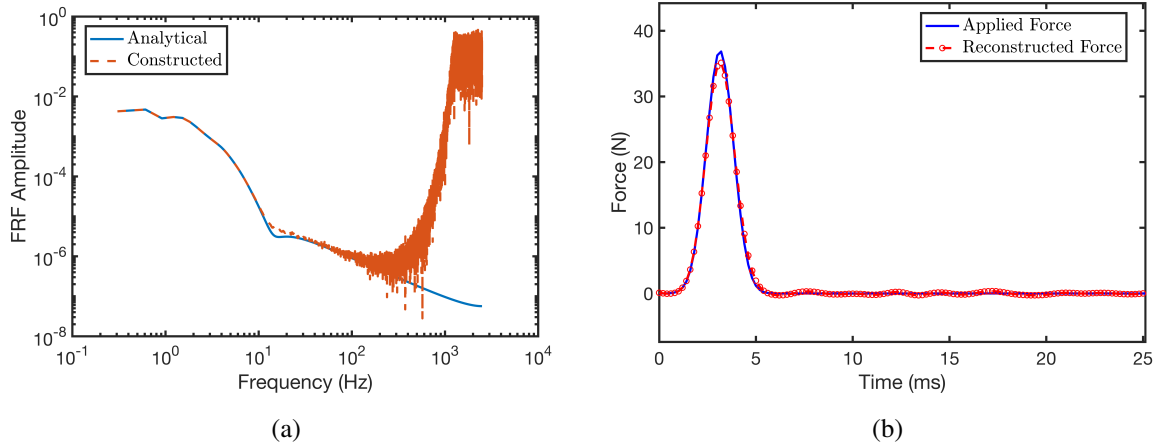


Figure 11: FRF solved SIMO FDIM noisy force reconstruction with ten calibration tests at same input. FRF at DOF 5 (a) and reconstructed force (b) are both shown. SNR= 150 used for this example.

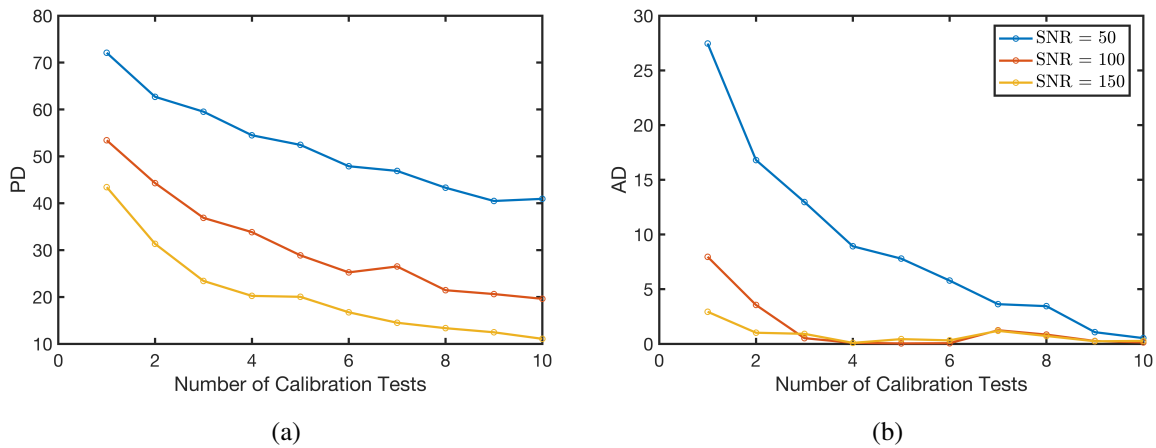


Figure 12: Peak (a) and Area (b) Difference versus number of calibration tests for FDIM SIMO numerical studies

on the area difference is more dramatic at lower SNR. Interestingly, the same accuracy with ten repeats for the SNR= 50 case is achieved as with a single test from a data set with a third the noise level. Clearly performing repeat tests can reduce the ill effects of noise.

3.5 MIMO Example

In this section the FDIM's ability to reconstruct pulses for the multiple input multiple output (MIMO) case is validated. The same ten DOF system discussed in the previous section is used. However, this time pulses are applied simultaneously at multiple locations. For this study all outputs (i.e. $n = 10$) and inputs at four locations (i.e. $p = 4$) are considered. Performing the FRF solved FDIM with no repeat tests or noise, the results in Figure 13 are obtained.

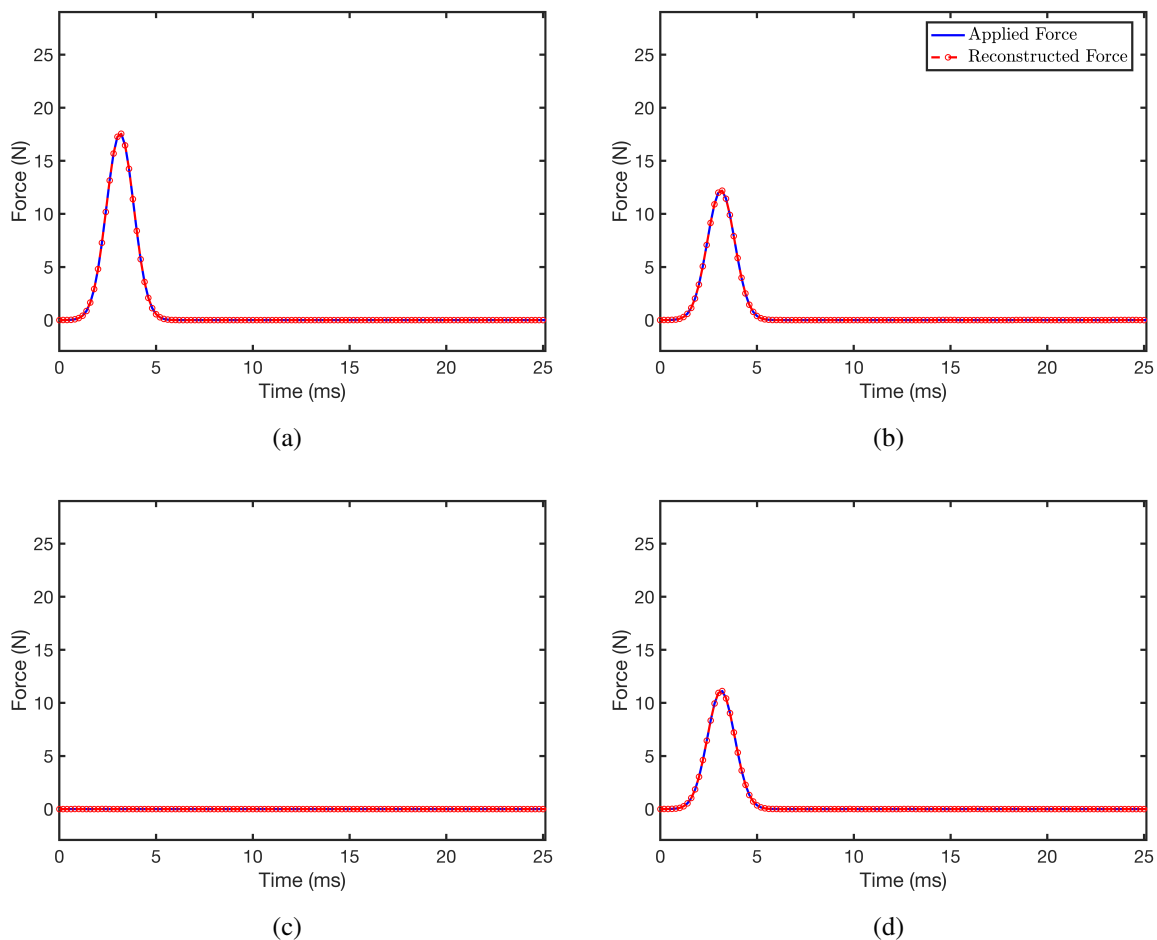


Figure 13: MIMO hammer pulse reconstruction for 10 DoF system. Applied force reconstruction at input nodes 2 (a), 4 (b), 6 (c), and 8 (d) are all shown. The FRF solved FDIM with no noise and $f_s = 5$ kHz were used for this study.

Note the high accuracy of the reconstructions for this MIMO case study. All three simultaneously applied input pulses have been accurately reconstructed. Additionally, the hole location with no applied load was correctly reconstructed as well.

Next it is of interest to investigate the effects of noise. Adding Gaussian noise to all output data at $\text{SNR} = 150$, the results in Figure 14 are obtained. This figure reveals that the FRF solved FDIM

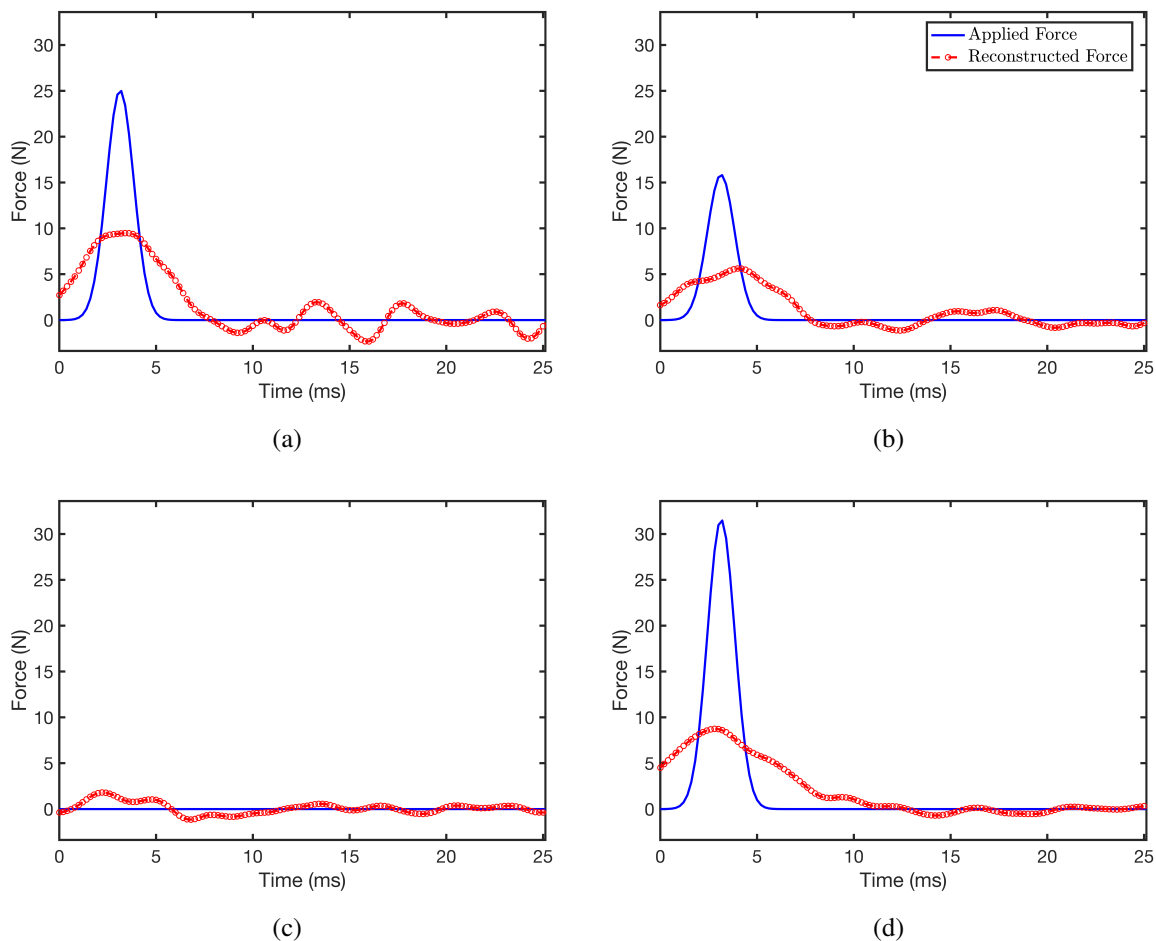


Figure 14: MIMO hammer pulse reconstruction for 10 DoF system. Applied force reconstruction at input nodes 2 (a), 4 (b), 6 (c), and 8 (d) are all shown. The FRF solved FDIM with $\text{SNR} = 150$ and $f_s = 5$ kHz were used for this study.

does a very poor job at reconstructing the pulse. Both the peak and width of the reconstructed pulses are highly inaccurate.

Next, one may investigate the influence of performing multiple calibration sets on the accuracy of the reconstruction. Note that since the accuracy of multiple input locations is of interest, a new set of error metrics are considered. These are defined as

$$\overline{\text{AD}} = \frac{1}{P_a} \sum_{i=1}^{P_a} \text{AD}_i \quad (36)$$

$$\overline{PD} = \frac{1}{P_a} \sum_{i=1}^{P_a} PD_i \quad (37)$$

where P_a is the number of locations where a force was applied. Therefore the accuracy of the zero load location is not considered. For the example case depicted in Figure 15, $P_a = 3$. For each of these locations, the area and peak difference are computed using Eqs. (34) and (35), respectively and then the results are averaged. The averaged peak and area differences versus number of calibration tests is depicted in Figure 15.

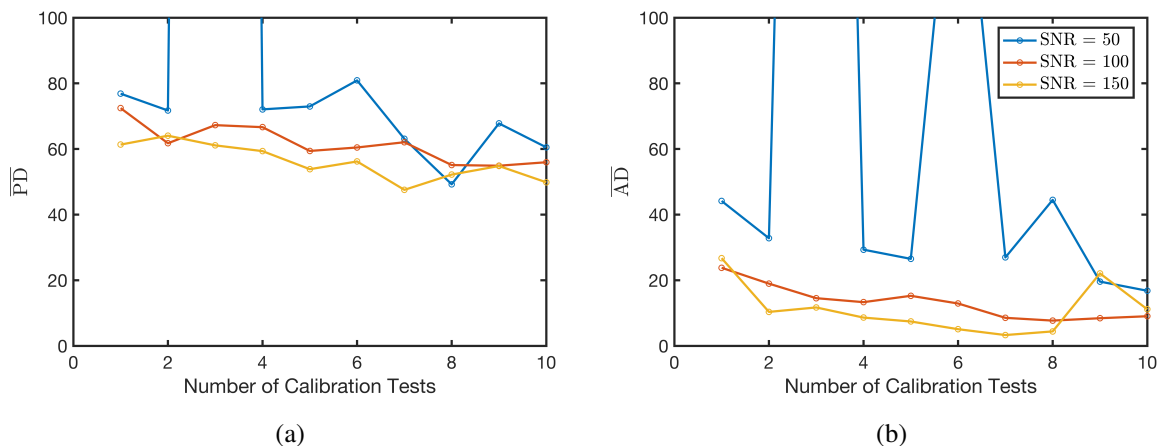


Figure 15: Peak (a) and Area (b) Difference averaged over each application location versus number of calibration tests for FDIM MIMO numerical studies

Interestingly, the results aren't nearly as drastic as in the SIMO case study. Although some improvement is observed in the peak and area difference as the number of input calibration tests increases, the effect is much smaller and never reaches a very low level of error (e.g. $< 10\%$ AD and PD). Additionally, the MIMO case study seems much more sensitive as compared to that of the SIMO. For the high noise case, the solution occasionally blows up. Clearly imposing the added constraint on the FRF solution (i.e. additional calibration input tests) is not enough to adequately reduce the ill conditioning in the force reconstruction solution for the MIMO case.

3.6 Acceleration Deconvolution

The final FDIM investigation is deconvolution of acceleration data. This section only considers the SISO system case. However, further experimental investigations demonstrate some of the advantages for the SIMO and MIMO cases.

Consider the numerical system shown in Figure 2. Assume the displacement and acceleration of this mass is measured. Next, a known load such as a pulse is applied to this system and the resultant response is recorded. The acceleration and known applied force can be used in conjunction with Eq. (21) to solve for the resultant acceleration FRF, \ddot{H} . For this example, consider the more simplified case where no repeat tests are used (i.e. $p = 1$). An acceleration IRF construction using this approach is displayed in Figure 16a. Next, the FRF can be used to solve for an applied

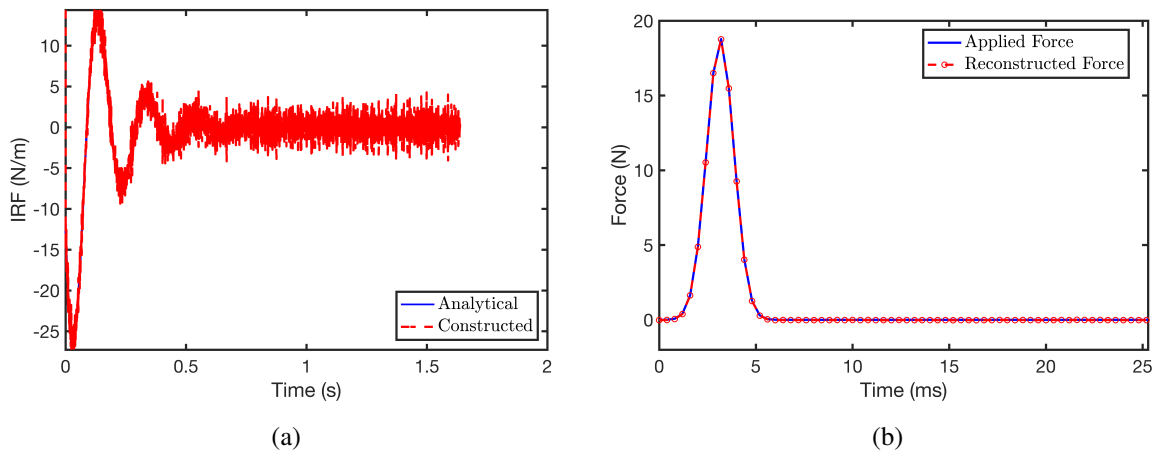


Figure 16: Acceleration IRF construction (a) and pulse force reconstruction (b) using FDIM acceleration deconvolution. SISO system with $\text{SNR} = 150$ used for these studies.

force given a measured dynamic acceleration response. An example pulse force reconstruction is displayed in Figure 16b. Note the excellent pulse reconstruction even with these noisy signals.

As noted in Section 2.4, this can be combined with the displacement data to reconstruct an applied load. A comparison pulse force reconstruction considering displacement-only, acceleration-only, and combined acceleration-strain deconvolution is shown in Figure 17.

Interestingly, the acceleration-only and combined acceleration-displacement deconvolution far outperform the displacement-only deconvolution. All methods perform well with no added noise. Therefore, the presence of noise appears to be more detrimental to the displacement deconvolution than acceleration. Future studies should be performed to determine the cause of this difference.

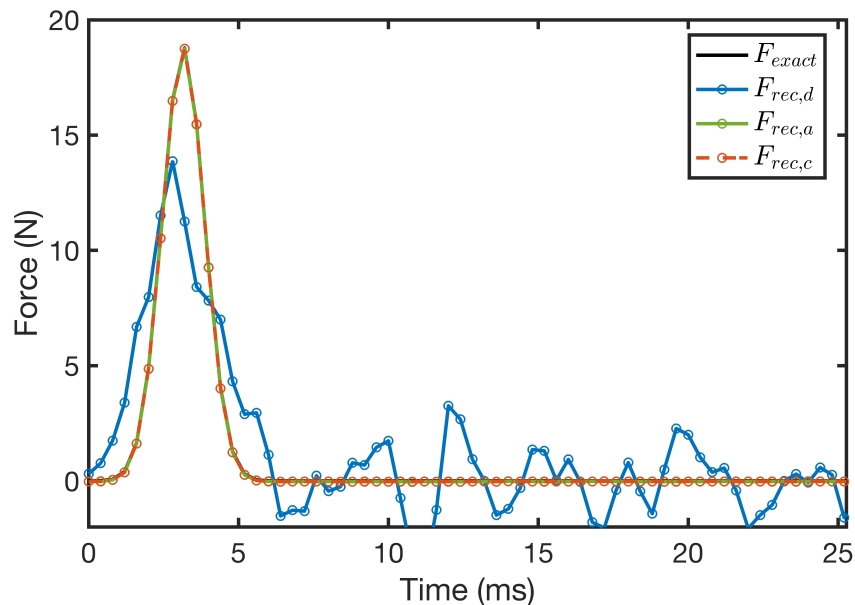


Figure 17: Pulse force reconstruction for acceleration-only ($F_{rec,a}$), displacement-only ($F_{rec,d}$), and combined acceleration-displacement ($F_{rec,c}$) deconvolution SISO example. The FDIM with $f_s = 2500$ Hz, and $SNR = 150$ used for this example.

4 Experimental Validation

In this section, the FDIM is validated on a test article in the Balance Calibration Laboratory at AEDC White Oak. In this section only the alterations of the FDIM: the FRF solved version and using multiple input tests at the same location are of interest. The majority of this section considers strain data as the output. However, the acceleration response is also used to quantify some trends about the method.

4.1 Experimental Setup

To create a test setup that closely resembled that of a tunnel run, a similarly sized test article was developed. The fully assembled model can be seen in Figure 18. This test article, designed by Collopy et al[1], was chosen to maximize the number of orthogonal loading locations and simulates the approximate size, weight, and natural frequencies of typical test articles used in Tunnel 9. A steel plate is affixed to the test article that has mounting holes for the load cells.

The strain sensors, discussed in a later section, must be constrained between the model and

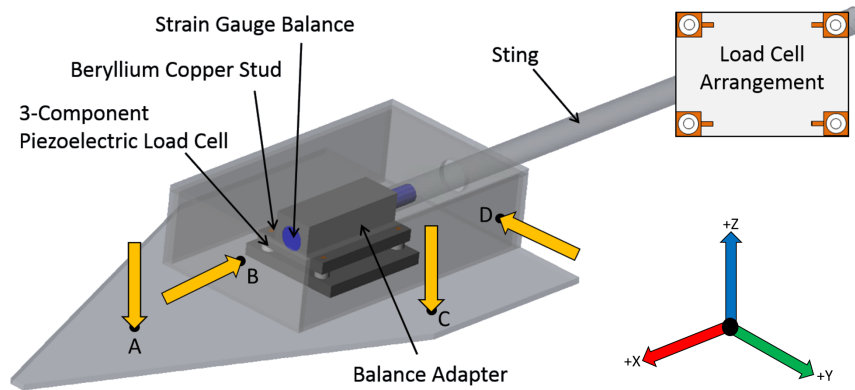


Figure 18: CAD representation of dynamic calibration bench top test article with sample input locations

sting to ensure the load travels through the sensors. For this reason, the strain sensors are mounted between the balance adapter (which connects to the sting) and the model. One may note that only a single load path exists between the model and support structure which passes through the sensors. Any other load path may inhibit the sensors performance.

The primary support structure used in most of the experimental studies is shown in Figure 19.

4.2 SIMO FDIM Experimental Results

Using the repeat formulation discussed in Section 2.3, a sample result shown in Figure 20 is obtained. As expected, excellent pulse reconstruction is observed and this accuracy is characteristic of the other hole locations. Four of the sample hole locations are displayed in Figure 18. The hole locations were chosen to orthogonal one of the three axes and spanning most of the test article. Eleven to fourteen calibration tests were performed at each hole. As discussed in Section 3.4, adding these tests during calibration should improve reconstruction accuracy.

To further justify the need of using multiple calibration tests at a single hole, the above analysis is repeated with a varying number of calibration tests. All 188 test pulses are reconstructed at each step and the average and max of each are recorded. When plotting these error metrics, as depicted in Figure 21 versus the number of calibration tests used to generate the FRF, a clear trend is observed. As in Section 3.4, it is clear that additional calibration loads substantially improve the performance of this method.



Figure 19: Calibration test article mounted on support structure

4.3 MIMO FDIM Experimental Results

The most difficult force reconstruction case is MIMO. This section details the validation of the FDIM MIMO force reconstruction using the same data set from the previous section. The capability to supply multiple loads simultaneously is not possible with our current equipment. However, one may still perform a MIMO reconstruction but expect zero reconstructed load at each location other than the application location.

An example MIMO reconstruction using the hole locations depicted in Figure 18 is shown in Figure 22.

Next, it may be of interest to see the effects of number of input locations, p on the accuracy of the reconstruction. To demonstrate this, the number of input locations are varied from one to fifteen. During each study, the MIMO FDIM is used to reconstruct the force contributions at each input location as is seen in Figure 22. Next, the peak and area difference of the reconstruction at the application location is computed and recorded. The mean and maximum of these peak and area differences are depicted versus number of input locations in Figure 23.

Several interesting conclusions can be drawn from Figure 23. First, there is a clear decline in performance as the number of input locations increases. This is expected as the inversion at

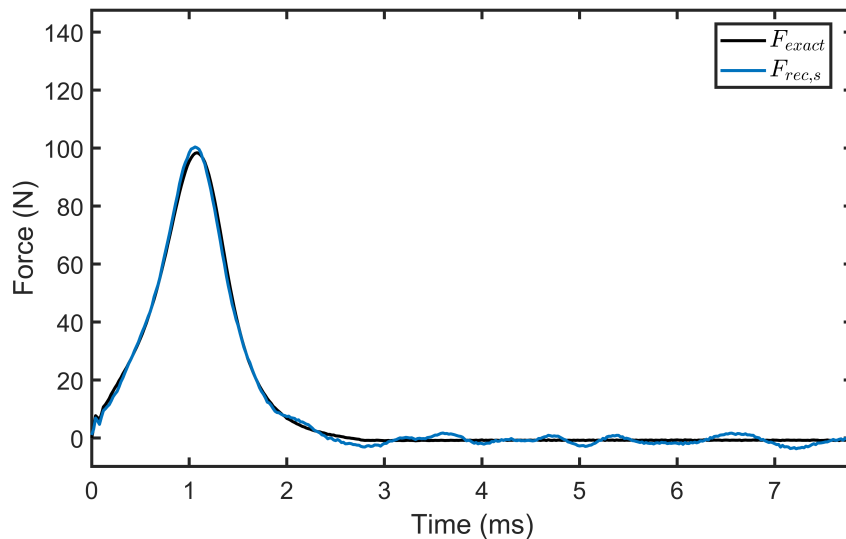


Figure 20: FDIM SIMO force reconstruction experimental example result. Eleven calibration input tests used for this reconstruction.

each frequency becomes closer to a square matrix. This method appears extremely effective at reconstructing the pulse even when multiple input locations are of interest. Interestingly, even when the number of inputs exceeds the number of outputs (i.e. $p > 12$), the FDIM still adequately reconstructs the input pulses.

4.4 Acceleration Deconvolution

As discussed previously in this paper, deconvolution of acceleration data is also an option for FDIMs. Many advantages of acceleration deconvolution exist such as ease of implementation. In this section, acceleration deconvolution and combined acceleration-strain deconvolution are validated for the experimental system.

First the SIMO case study discussed in Section 4.2 is repeated but we consider strain-only, acceleration-only, and combined acceleration-strain deconvolution. An example result is shown in Figure 24. Note the excellent reconstruction accuracy of all three deconvolution variants. No obvious advantage of one method over another is observed.

It is important to quantify the accuracy across all tests. Therefore, the peak and area difference for each deconvolution variant across all 188 reconstructions is computed. The maximum number of available calibration tests per hole were used. This ranges from eleven to fourteen depending on

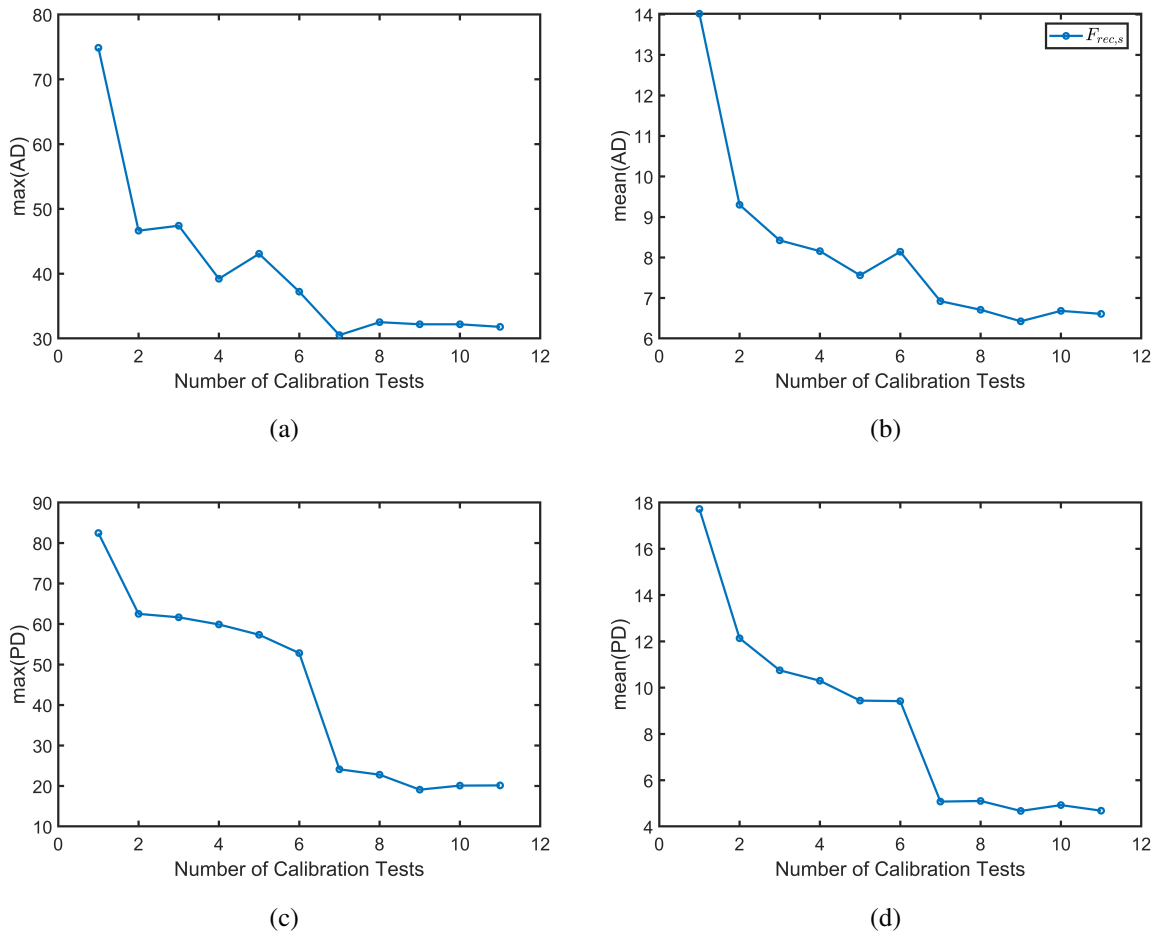


Figure 21: Area and peak difference of FDIM input pulse force versus number of calibration tests. Max area (a), average area (b), max peak (c), and average peak (d) difference are all shown.

the hole location. These results are presented in Table 1.

Upon review of Table 1, it is clear that all three deconvolution variants perform admirably for the SIMO case study. The FDIM with multiple calibration input solution of the FRF is extremely effective for SIMO pulse reconstruction.

Next, the study shown in Figure 21 is repeated. The results for acceleration-only, strain-only, and combined acceleration-strain deconvolution are shown in Figure 25. Again, a trend between accuracy and number of calibration inputs is observed for each deconvolution variant. Clearly, using more calibration inputs improves the accuracy of the reconstruction. Interestingly, no clear advantage is observed between the three variants.

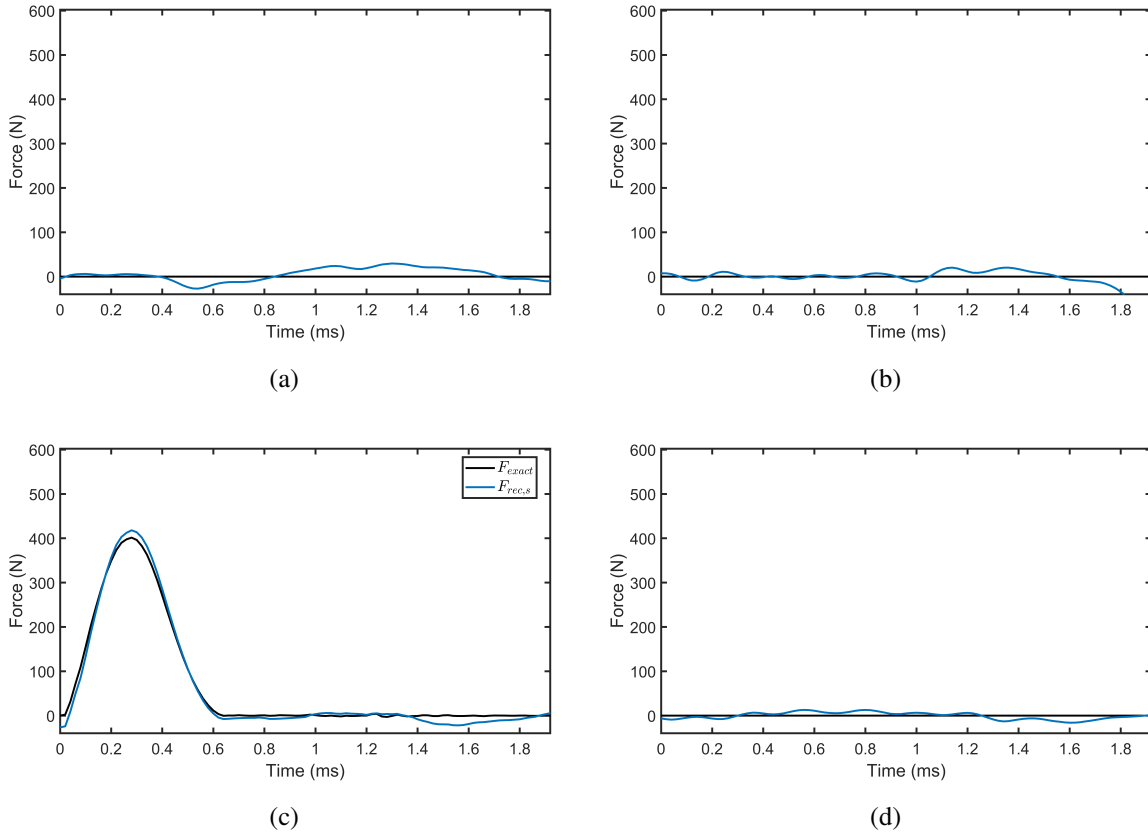


Figure 22: FDIM MIMO force reconstruction of point load applied at location C. A sampling rate of 50 kHz was used. Reconstructions at hole locations A (a), B (b), C (c), and D (d) shown in Figure 18 are all shown.

Table 1: Peak and area differences for strain-only, acceleration-only, and combined strain-acceleration FDIM force reconstruction.

	Maximum			Average		
	S	A	C	S	A	C
AD	46.75	37.91	31.80	6.69	6.96	6.59
PD	28.12	22.90	19.55	4.76	5.55	4.64

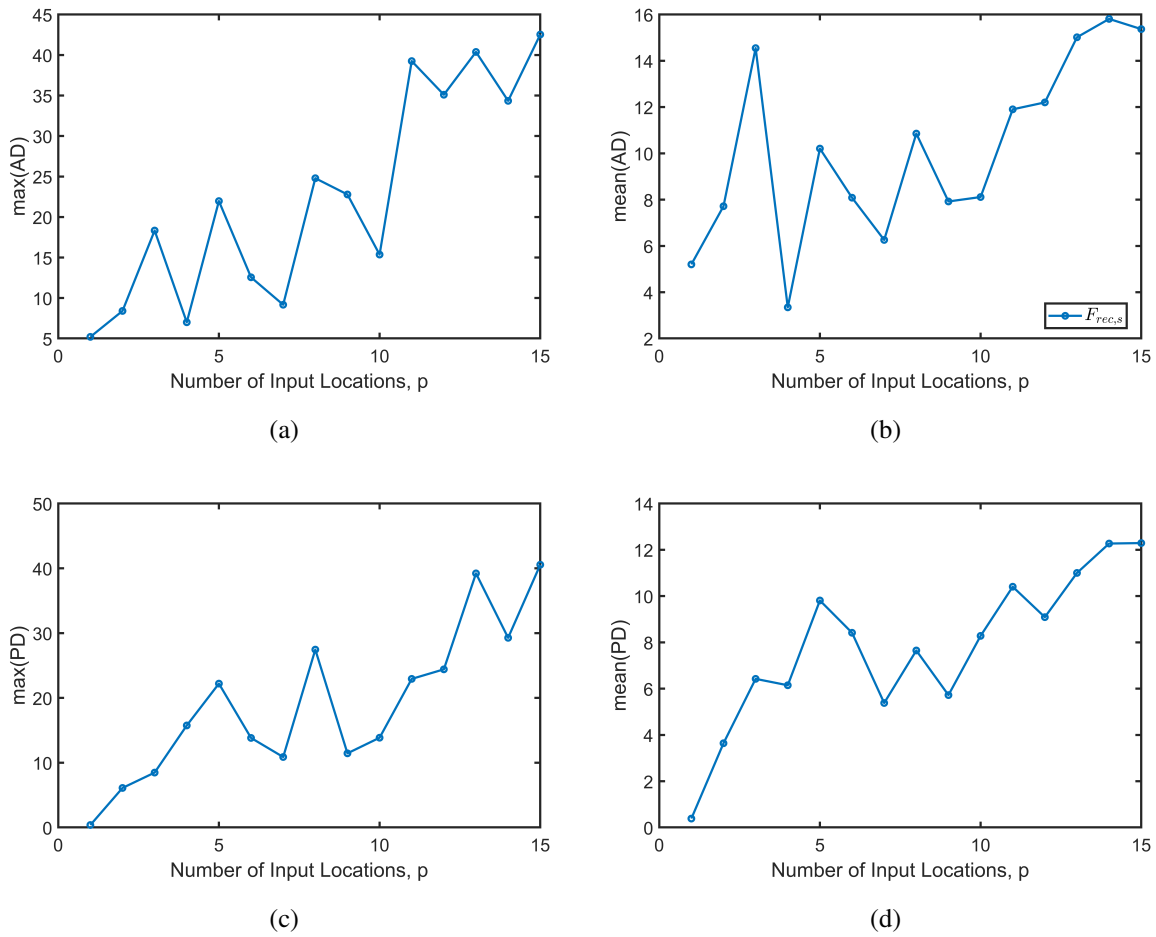


Figure 23: Area and peak difference of input pulse force versus number input locations using the FDIM MIMO formulation. Max area (a), average area (b), max peak (c), and average peak (d) difference are all shown.

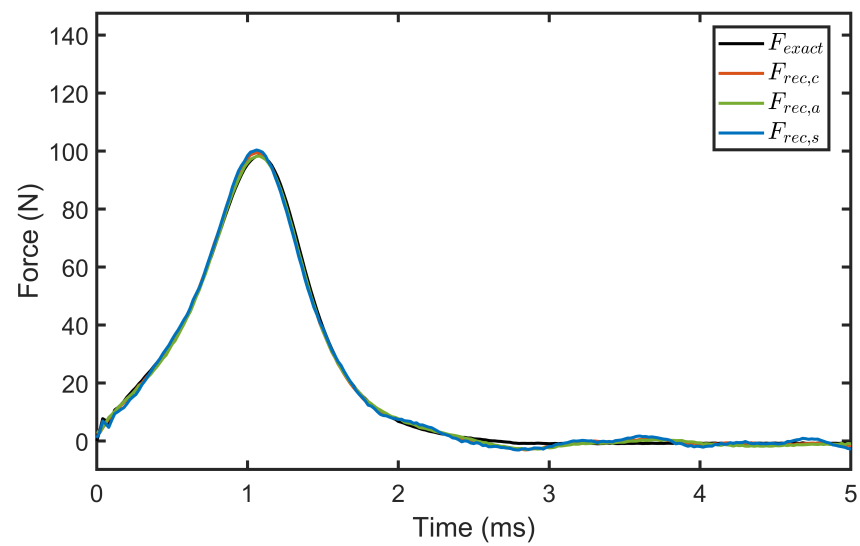
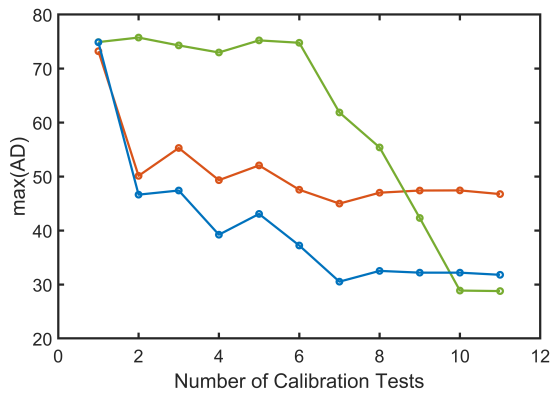
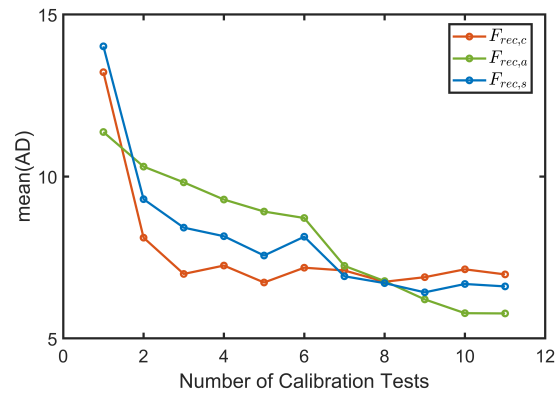


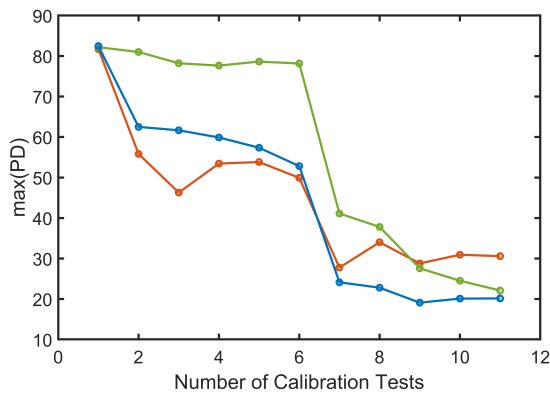
Figure 24: FDIM SIMO acceleration deconvolution force reconstruction experimental example result. Eleven calibration input tests used for this reconstruction.



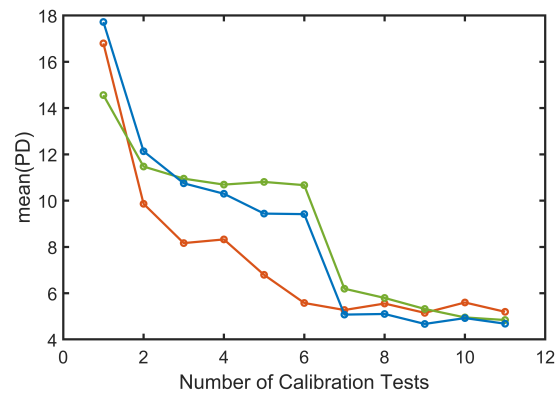
(a)



(b)



(c)



(d)

Figure 25: Area and peak difference of FDIM input pulse force versus number of calibration tests. Max area (a), average area (b), max peak (c), and average peak (d) difference are all shown. Acceleration-only, strain-only, and combined acceleration-strain deconvolution are all shown.

5 Conclusions

In this work, several alterations to the conventional FDIM were formulated. Most notably, the use of multiple calibration inputs at a particular location to reduce the ill effects of noise and user error. Additionally, the applicability of the FDIM was extended to acceleration measurements which have a number of advantages in the dynamic case such as larger response magnitudes and ease of implementation.

These alterations were first validated on SISO, SIMO, and MIMO numerical systems. These proved the validity of the alterations and served to highlight the advantage of increasing accuracy with increased number of repeat tests at a particular location.

Finally, these alterations were validated on an experimental system in AEDC's Balance Calibration Laboratory. This demonstrated the method's effectiveness on a real system with measurement noise and user error.

Future work will include the reconstruction of dynamic applied loads such as ramp-step and loads applied to a wind tunnel test article where the applied load is not measured directly. Additionally, the quantification of uncertainties is also a topic for future research. Results from this work will be used to support future dynamic wind tunnel tests at AEDC Tunnel 9.

6 Acknowledgments

The work presented in this paper was funded through Arnold Engineering Development Complex at White Oak, MD. Task Order: 17-01.

References

- [1] Arianne Collopy, Sung Lee, and Eric C. Marineau. Development of Dynamic Force Measurement Capabilities at AEDC Tunnel 9. American Institute of Aeronautics and Astronautics, January 2014.
- [2] John W. Draper, Sung Lee, and Eric C. Marineau. Development and Implementation of a Hybrid Dynamic Force Measurement System at AEDC Tunnel 9. American Institute of Aeronautics and Astronautics, January 2017.
- [3] J.W. Draper, S.W. Lee, and E.C. Marineau. Numerical construction of impulse response functions and input signal reconstruction. *Journal of Sound and Vibration*, 432:259–271, October 2018.
- [4] J.W. Draper III and S.W. Lee. Smooth construction of impulse response functions and applied loads using a time domain deconvolution method. *Journal of Sound and Vibration*, 443:430–443, March 2019.
- [5] Nathan Falkiewicz, Carlos Cesnik, Michael Bolender, and David Doman. Thermoelastic Formulation of a Hypersonic Vehicle Control Surface for Control-Oriented Simulation. In *AIAA Guidance, Navigation, and Control Conference*, Chicago, Illinois, August 2009. American Institute of Aeronautics and Astronautics.
- [6] J. L. Grunnet. Factors affecting the magnitude of jet interaction forces. *Journal of Spacecraft and Rockets*, 8(12):1234–1235, December 1971.
- [7] Internal Balance Technology Working Group, editor. *Recommended Practice: Calibration and Use of Internal Strain-Gage Balances with Application to Wind Tunnel Testing (AIAA R-091-2003)*. American Institute of Aeronautics and Astronautics, Inc., Washington, DC, January 2003.
- [8] Mitsuru Kurita, Tsuyoshi Inoue, and Yoshiaki Nakamura. Aerodynamic interaction due to side jet from a blunted cone in hypersonic flow. American Institute of Aeronautics and Astronautics, August 2000.

- [9] John F. Lafferty, Joseph J. Coblish, Eric Marineau, Joseph D. Norris, Inna Kurits, Daniel R. Lewis, Michael Smith, and Michael Marana. The Hypervelocity Wind Tunnel No. 9; Continued Excellence Through Improvement and Modernization. American Institute of Aeronautics and Astronautics, January 2015.
- [10] Stuart Laurence, Jan Martinez Schramm, Sebastian Karl, and Klaus Hannemann. An Experimental Investigation of Steady and Unsteady Combustion Phenomena in the HyShot II Combustor. American Institute of Aeronautics and Astronautics, April 2011.
- [11] Stuart Laurence, Hiroshi Ozawa, Damien Lieber, Jan Martinez Schramm, and Klaus Hannemann. Investigation of Unsteady/Quasi-Steady Scramjet Behavior using High-Speed Visualization Techniques. American Institute of Aeronautics and Astronautics, September 2012.
- [12] Andrew Lazur, J. Sawyer, Brian Sullivan, and Larry Hudson. Hypersonic vehicle control surface development. In *9th International Space Planes and Hypersonic Systems and Technologies Conference*, Norfolk, VA, U.S.A., November 1999. American Institute of Aeronautics and Astronautics.
- [13] Eric Marineau, Matthew MacLean, E. Mundy, and Michael Holden. Force Measurements in Hypervelocity Flows with an Acceleration Compensated Strain Gage Balance. *Journal of Spacecraft and Rockets*, 49(3):474–482, May 2012.
- [14] Eric C. Marineau. Force Measurements in Hypervelocity Flows with an Acceleration Compensated Piezoelectric Balance. *Journal of Spacecraft and Rockets*, 48(4):697–700, July 2011.
- [15] D. J. Mee. Dynamic calibration of force balances for impulse hypersonic facilities. *Shock Waves*, 12(6):443–455, May 2003.
- [16] David J. Mee, William J. T. Daniel, and John M. Simmons. Three-component force balance for flows of millisecond duration. *AIAA Journal*, 34(3):590–595, March 1996.
- [17] Christina Ngo, Jessica Powell, and James C. Ross. Inverse Force Determination on a Small Scale Launch Vehicle Model using a Dynamic Balance. In *55th AIAA Aerospace Sciences*

Meeting, Grapevine, Texas, January 2017. American Institute of Aeronautics and Astronautics.

- [18] M. L. G. Oldfield. Impulse Response Processing of Transient Heat Transfer Gauge Signals. *Journal of Turbomachinery*, 130(2):021023, 2008.